SOLA (2026) 22:27
https://doi.org/10.1007/s44393-026-00024-0

BRIEF REPORT

Multiscale Aspects of an Extreme Precipitation Event over Nepal in September 2024

Hatsuki Fujinami[1] · Nobuhiro Takahashi[1] · Hironari Kanamori[2] · Yota Sato[3] · Sojiro Sunako[4] · Masaya Kato[1] · Atsushi Higuchi[5,6,7] · Indira Kadel[8] · Dibas Shrestha[9] · Rijan B. Kayastha[10] · Koji Fujita[11]

Received: 30 December 2025 / Accepted: 20 April 2026

Abstract

On 26–28 September 2024, torrential rainfall struck Nepal during the late monsoon season, causing flooding, landslides and extensive damage. This study examined the multiscale processes contributing to this extreme precipitation event, focusing on intraseasonal oscillations, synoptic-scale circulations, and mesoscale cloud/precipitation systems. A quasi-biweekly intraseasonal oscillation dominated over South Asia during the event, featuring a monsoon low-pressure system over the Indian Peninsula and an anticyclone to its east, both propagating westward. The pressure gradient between them sustained strong southerly moisture transport toward the Himalayas, establishing a persistently humid environment and orographic lift along the southern slopes. In contrast to reports of previous extreme precipitation events in Nepal, the atmospheric circulation responsible for the 2024 event was primarily of tropical origin, with minimal influence from the midlatitudes. Characteristic mesoscale cloud/precipitation systems also developed around the Himalayas. The highest daily precipitation during the event was recorded on 27 September; stratiform systems with relatively modest storm top heights developed over the southern slopes, generating surface precipitation rates of >100 mm h^{-1} through warm-rain processes. Rain gauges across the glacierized basin (3500–5000 m asl) recorded exceptionally high daily and hourly precipitation rates, highlighting the extension of intense rainfall to unusually high elevations.

Keywords Himalayas · Extreme precipitation event · Intraseasonal oscillations · Low pressure systems · Mesoscale convective systems

✉ Hatsuki Fujinami
hatsuki@nagoya-u.jp

1 Institute for Space-Earth Environmental Research, Nagoya University, Furo-cho, Chikusa-ku, Nagoya 464-8601, Japan

2 Faculty of Business Administration, Kobe Gakuin University, 1-1-3 Minatojima, Chuo-ku, Kobe 650-8586, Japan

3 Institute of Science and Technology Austria, Am Campus 1, Klosterneuburg 3400, Austria

4 Snow and Ice Research Center, National Research Institute for Earth Science and Disaster Resilience, 187-16 Maeyama, Suyoshi-cho, Nagaoka 940-0821, Japan

5 Center for Environmental Remote Sensing, Chiba University, 1-33 Yayoi- cho, Inage-ku, Chiba 263-8522, Japan

6 Research Institute of Disaster Medicine, Chiba University, 1-8-1 Inohana, Chuo-ku, Chiba 260-0856, Japan

7 Typhoon Science and Technology Research Center, Yokohama National University, 79-5 Tokiwadai, Hodogaya-ku, Yokohama 240-8501, Japan

8 Department of Hydrology and Meteorology, Babarmahal, Kathmandu, Nepal

9 Central Department of Hydrology and Meteorology, Tribhuvan University, Kirtipur, Kathmandu, Nepal

10 Department of Environmental Science, School of Science, Kathmandu University, Dhulikhel, Nepal

11 Graduate School of Environmental Studies, Nagoya University, Furo-cho, Chikusa-ku, Nagoya 464-8601, Japan

Published online: 04 June 2026

1 Introduction

On 26–28 September 2024, devastating late monsoon precipitation resulted in severe flooding and landslides across Nepal, causing 250 fatalities and losses exceeding 1% of the country's Gross Domestic Product (Lamichhane et al. 2025). On 27 September, new 24-h precipitation records were set across 25 rain gauge stations (Department of Hydrology and Meteorology 2024).

Low pressure systems (LPSs) forming over the Bay of Bengal, midlatitude troughs and their interactions have been identified as primary factors causing heavy rainfall events in the Himalayas during summer; these elements in the synoptic-scale circulation result in the concentration of strong low-level winds toward the Himalayan slopes, enhancing the forced uplift of humid air (Bohlinger et al. 2017, 2019; Fujinami et al. 2025; Hirata et al. 2023; Houze et al. 2017; Vellore et al. 2016). However, the primary cause of the extreme precipitation event in September 2024 remains unclear.

Typically, heavy rainfall over the Himalayas is associated with vertically extensive convective systems such as mesoscale convective systems and cloudbursts (Bohlinger et al. 2019; Das et al. 2006; Dimri et al. 2017) as well as stratiform-type precipitation systems (Houze et al. 2017). The characteristics of these systems vary with atmospheric conditions and can be studied effectively using continuous observations from ground-based precipitation radars. Although such radars have been installed in Nepal in recent years (Talchabhadel et al. 2022), the data are not yet publicly available for research purposes. Conversely, observations from space-borne precipitation radars are readily available and can be used to study the three-dimensional structure of these event-based precipitation systems.

In Nepal, most rain gauges are located at low–mid elevations (Bohlinger et al. 2017; Sharma et al. 2020); very few are at high elevations (>3000 m asl). Data from gauges in high-elevation areas, including in the vicinity of glaciers, are critically important because estimates of precipitation at high elevations based on satellites and spaceborne precipitation radars are associated with large uncertainties (Fujinami et al. 2021).

In this study, we investigated multiscale features—intraseasonal oscillations (ISOs), synoptic-scale circulation, and mesoscale cloud/precipitation systems, including terrain-induced convection—to identify the causes of the extreme precipitation event that occurred over Nepal during the late monsoon period of 2024. We analyzed the extreme precipitation at high-elevation areas (>3000 m asl), including in the vicinity of glaciers, using data from a rain gauge network in the Himalayas in eastern Nepal. While various human factors may have contributed to the floods and landslides triggered by this torrential rainfall event (Lamichhane et al. 2025), analysis and discussion of these factors are beyond the scope of this study.

2 Data and Method

To investigate the spatial distribution of precipitation across Nepal during 26–28 September 2024 we obtained data collected at 343 rain gauge stations from the Department of Hydrology and Meteorology (DHM) in Nepal. The definition of DHM's daily precipitation for Day N is the cumulative amount for 03:00 UTC of Day $N-1$ to 03:00 UTC of Day N. To ensure temporal consistency with other datasets, the 24-h cumulative precipitation value from the DHM was referred to as the 24-h precipitation value for Day $N-1$ in this study. To study extreme precipitation at high elevations, we employed data from rain gauges at Simigaun (2024 m asl), Beding (3761 m asl), Na (4183 m asl), and Trakarding Glacier (4806 m asl), deployed by the authors in the Rolwaling region (Hirata et al. 2023), and from one rain gauge at the Pyramid observatory (5035 m asl) in the Khumbu region of the Himalayas of eastern Nepal (Fig. 1b). Hourly (total precipitation in the preceding hour) and daily (total precipitation from 00:00–24:00 UTC of the same day) data are available from these five stations.

We used infrared (channel 9: 10.8 μm) brightness temperature from the Spinning Enhanced Visible and Infrared Imager (SEVIRI) of Meteosat Second Generation-2 (MSG-2; Meteosat-9) (Schmetz et al. 2002) Indian Ocean Data Coverage (IODC) to examine cloud systems associated with the extreme precipitation event. Data were provided on a 0.04° latitude × 0.04° longitude grid with 15-min intervals. We also used the US National Oceanic and Atmospheric Administration (NOAA) Climate Prediction Center's daily blended outgoing longwave radiation (OLR) data on a 2.5° × 2.5° grid to detect large-scale convective activity.

To investigate precipitation characteristics, including vertical structure during the extreme precipitation event, we used near-surface precipitation rate, precipitation rate profile, storm top height, and precipitation type from the Global Precipitation Measurement (GPM) Dual-frequency Precipitation Radar (DPR) Ku-band (KuPR; 13.6 GHz) V07 product. The KuPR algorithm classifies rain pixels into three types: convective, stratiform, and other (Awaka et al. 2021; Seto et al. 2021). The horizontal resolution of the GPM KuPR is 5 km. For each swath, vertical distribution data were remapped onto a regular 0.05° × 0.05° grid with a vertical resolution of 125 m and horizontal data were remapped onto a 0.1° × 0.1° grid.

We used hourly European Centre for Medium-Range Weather Forecasts Reanalysis fifth-generation (ERA5) data

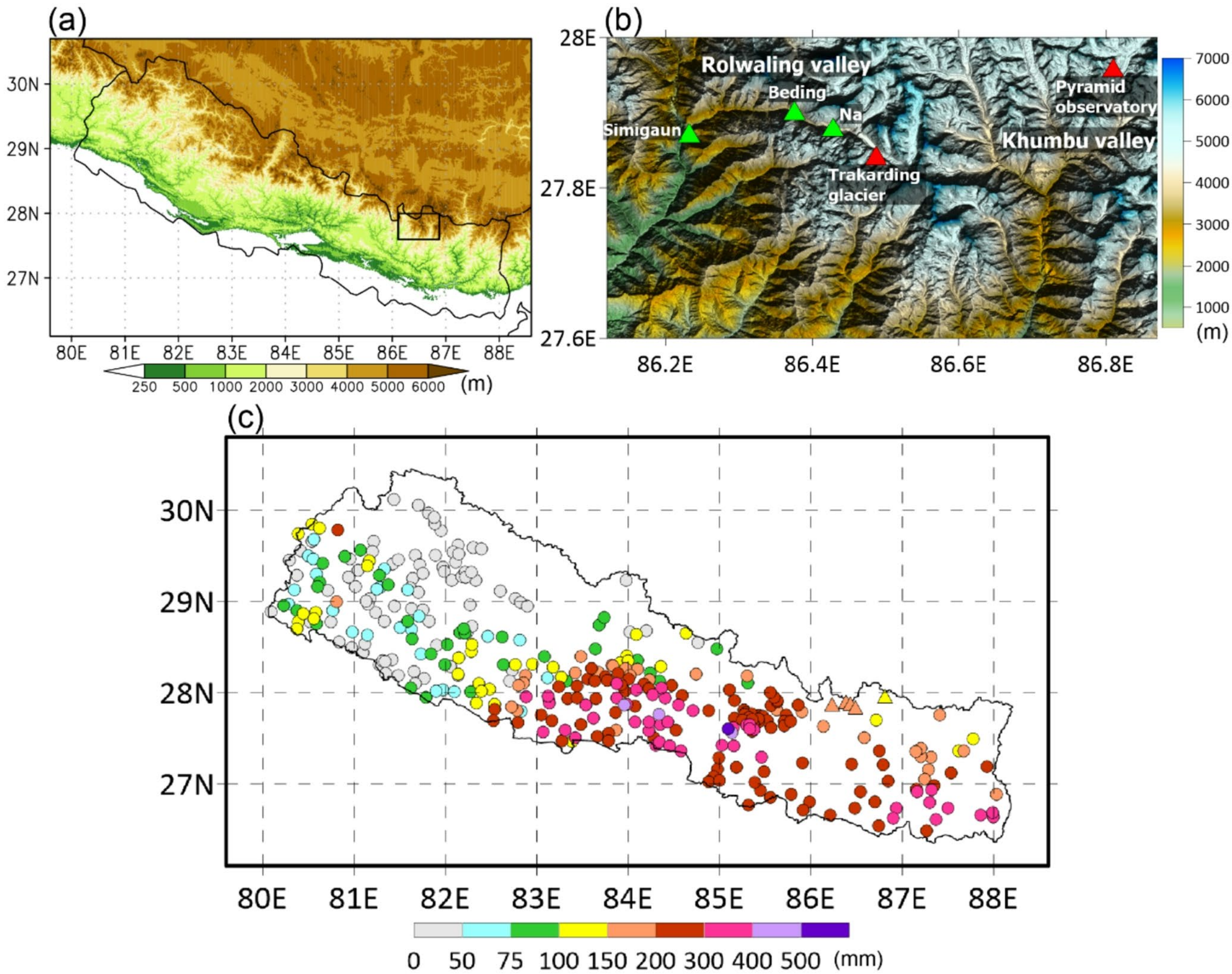

Fig. 1 (**a**) Topography around Nepal based on Global Multi-resolution Terrain Elevation Data (GMTED2010). The rectangle indicates the location of the Rolwaling and Khumbu regions in the Himalayas in eastern Nepal. (**b**) Topography and locations of the rain gauge stations in the Rolwaling and Khumbu regions. Green triangles represent tipping bucket rain gauge stations. Red triangles indicate stations with weighing rain gauges. (**c**) Total precipitation (mm) during 26–28 September 2024 based on surface rain gauge observations. Circles represent rain gauges of the Department of Hydrology and Meteorology (DHM) in Nepal. Triangles indicate rain gauges in (**b**)

on a 0.25° × 0.25° grid (Hersbach et al. 2020) to analyze atmospheric circulations during the event. Equivalent potential temperature was calculated following Bolton (1980). We also calculated streamfunction from horizontal winds.

We used a Rossby wave filter that is a bandpass filter in the frequency–wavenumber domain to detect $n=1$ equatorial Rossby (ER) waves (Kiladis et al. 2009; Masunaga 2007). We applied the ER wave filter used by Masunaga (2007) to detrended OLR anomalies with the seasonal cycle removed. To extract 10–20-day/quasi-biweekly (QBW) ISO, an 8–25-day Lanczos bandpass filter (Duchon 1979) was applied to the detrended anomalies (Fujinami et al. 2014).

3 Results and Discussion

3.1 Precipitation, Synoptic Conditions and ISOs During 26–28 September 2024

During 26–28 September, cumulative precipitation of >200 mm was recorded across central–eastern Nepal, particularly along the concave slopes at 83°–86° E; rainfall totals reached 300–500 mm at some locations (Fig. 1). At higher elevations, precipitation reached 187 mm at Simigaun, 193 mm at Beding, 168 mm at Na, 193 mm at the terminus of Trakarding Glacier, and 128 mm at the Pyramid observatory (triangles in Fig. 1c). Heavy precipitation moved from central to eastern Nepal between 26 and 28 September (Fig.

S1). It was concentrated around the concave slopes on 27 September and observed daily rainfall was 300–400 mm.

The extreme precipitation event of 26–28 September coincided with the transition from an LPS to an anticyclone over South Asia to the south of the Himalayas (Fig. 2b), creating a pressure gradient that sustained strong southerlies toward the Himalayas throughout the duration of the event. The slow westward movement of the pair of LPS and anticyclone throughout the troposphere (i.e., a barotropic-like structure) was a key feature during this extreme precipitation event; it led to a continuous massive inflow of water vapor onto the lower–upper southern slopes of the Himalayas, which sustained precipitation up to higher elevations (Figs. 2c–h and S2). Associated with this change, the water vapor flux (WVF) shifted from southeasterly to southwesterly. Cloud activity reached its maximum around the

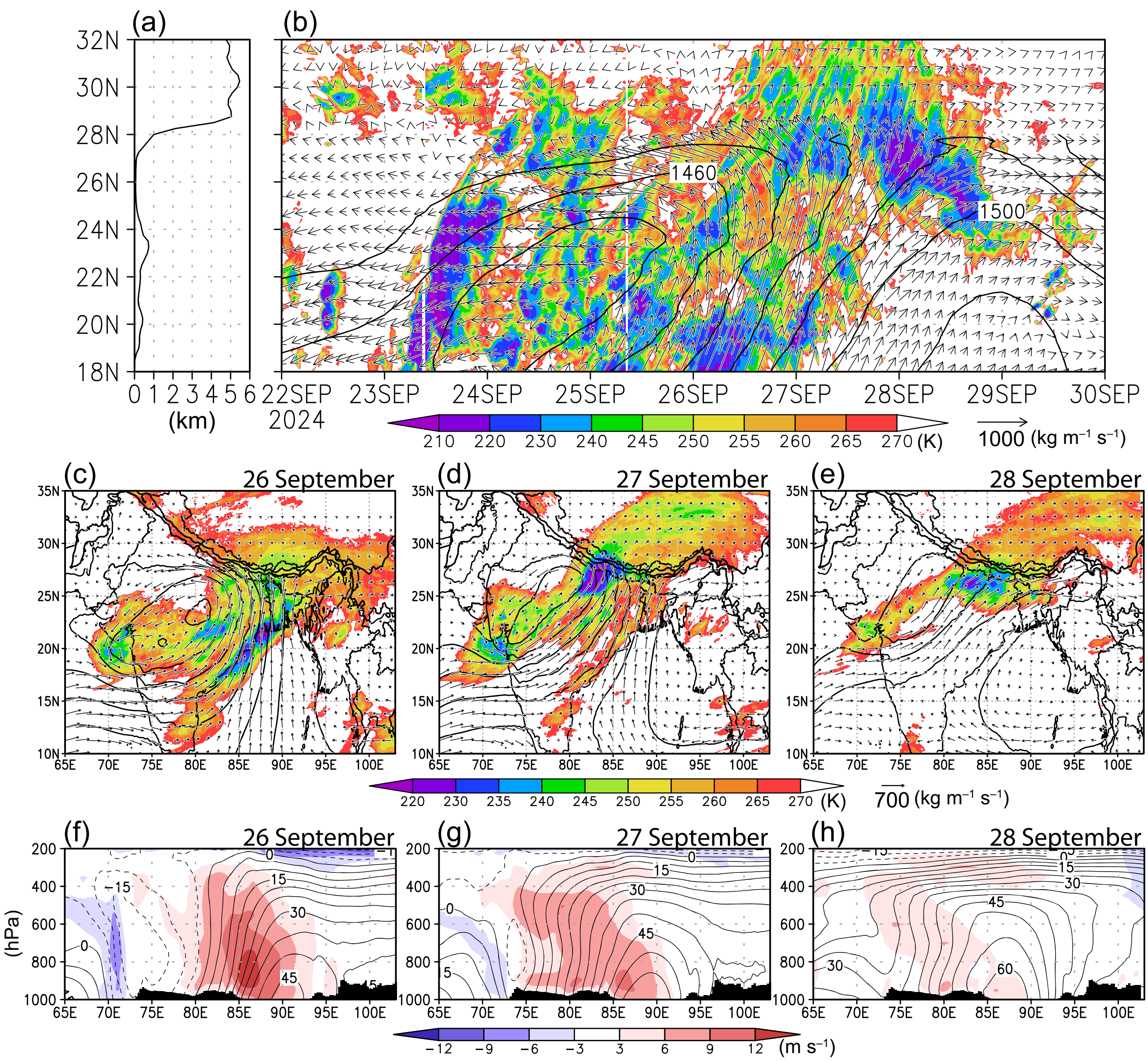

Fig. 2 (**a**) Average surface elevation between 84° and 85° E from European Centre for Medium-Range Weather Forecasts Reanalysis fifth-generation (ERA5) data (km asl). (**b**) Latitude–time section of infrared brightness temperature (shading; K), vertically integrated water vapor flux (vectors; kg m^{-1} s^{-1}), and 850-hPa geopotential height (contours; gpm) between 84° and 85° E. Contour interval for geopotential height is 10 gpm. The y-axis is the same as in (**a**). Horizontal distributions of infrared brightness temperature (shading; K), vertically integrated water vapor flux (WVF) (vectors; kg m^{-1} s^{-1}), and 850-hPa geopotential height (contours; gpm) are shown for (**c**) 26 September, (**d**) 27 September, and (**e**) 28 September 2024. Contour interval for geopotential height is 10 gpm. Height–longitude sections of geopotential height anomalies from seasonal mean (June–September 2024) (contours; gpm) and meridional wind component (shading; m s^{-1}) between 19° and 21° N for (f) 26 September, (**g**) 27 September, and (**h**) 28 September

southern slopes of the Himalayas on 27–28 September when the southwesterly WVF was perpendicular to the Himalayas. On 27 September, WVF from both the Arabian Sea and Bay of Bengal converged over the southern slopes of the Himalayas, creating extremely humid conditions with total column water exceeding 70 mm to the south of the Himalayas (Fig. S3a). The convergence of WVF over the concave Himalayan slopes resulted in heavy rainfall (Fig. S3b). Clouds formed around the Himalayas and extended as far as the northeastern Tibetan Plateau (Fig. 2b and d). Southward intrusion of a midlatitude trough or quasi-stationary Rossby waves along the Asian jet around the Himalayas/Tibetan Plateau were primary causes of past extreme rainfall events in the Himalayas; in 2024, these phenomena were absent from the middle–upper troposphere and fluctuations in the atmospheric circulation south of the Himalayas were dominant (Fig. S2).

The occurrence of the pair of synoptic-scale LPS and anticyclone over South Asia appears to be strongly influenced by ISOs, which originated in the Pacific and were on larger spatiotemporal scales (Fig. 3a). An area of active convection with a negative OLR anomaly around 80° E on 26 September was associated with the LPS to the south of the Himalayas, while an area of suppressed convection with a

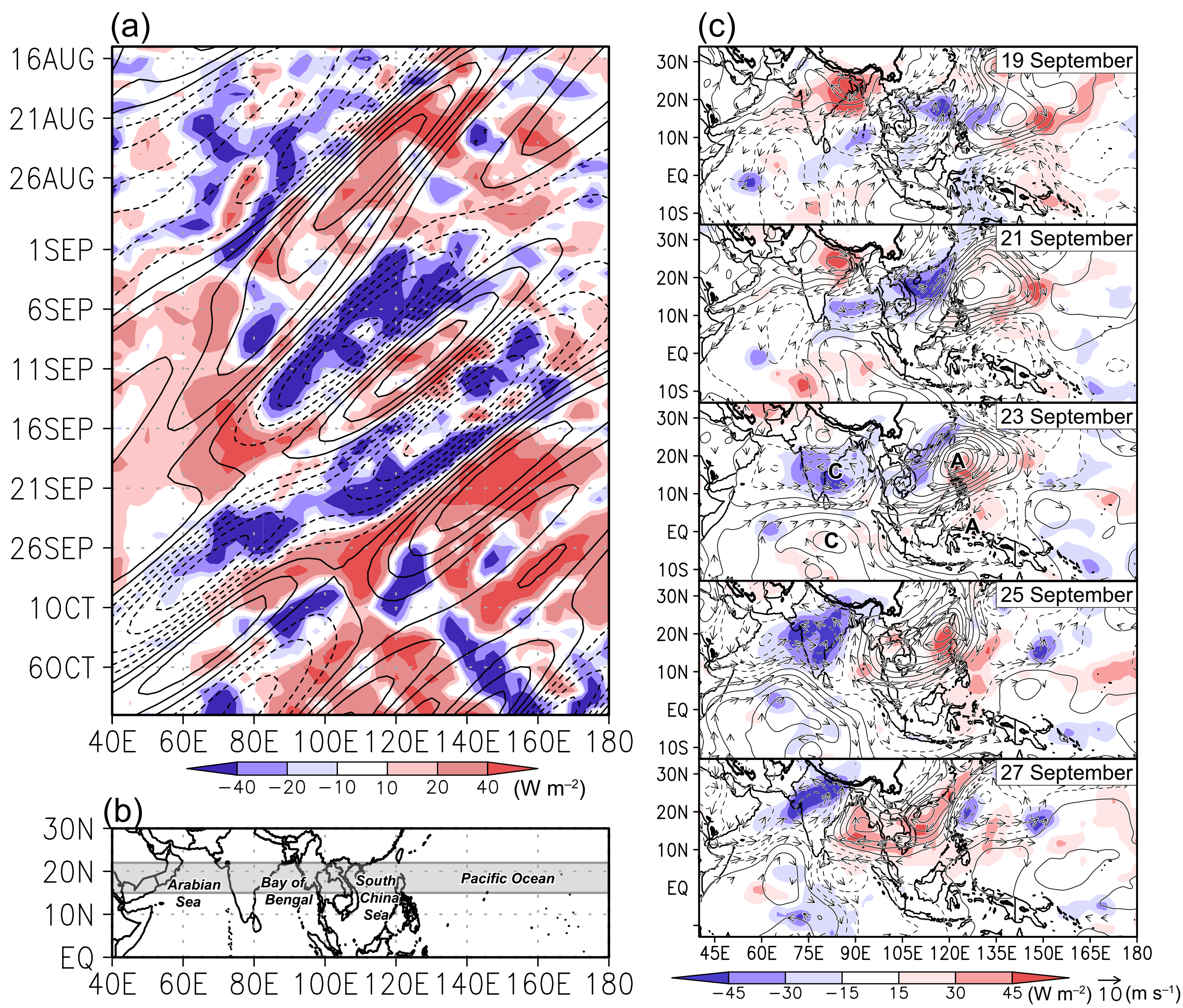

Fig. 3 (**a**) Time–longitude section of outgoing longwave radiation (OLR) anomaly (shading; W m^{-2}) and Rossby-wave-filtered OLR anomaly (contours; W m^{-2}) averaged over 15°–22.5° N, which is shaded in gray on the map in (**b**). The OLR anomaly was calculated by subtracting the seasonal cycle from the raw time series. Contour interval for the filtered OLR anomaly is 5 W m^{-2}. See the text for details of the Rossby wave filter. (**b**) A map of 0°–30° N, 40°–180° E. Details for the area shaded in gray are shown in (**a**). (c) 8–25-day filtered OLR anomaly (shading; W m^{-2}), 850-hPa streamfunction anomaly (contours; m^2 s^{-1}), and horizontal wind anomaly (vectors; m s^{-1}) for 19–27 September at 2-day intervals. Contour interval for streamfunction is 1×10^6 m^2 s^{-1}. Only vectors with wind anomalies of 2 m s^{-1} or greater are shown. For 23 September, C and A denote cyclonic and anti-cyclonic anomalies of interest, respectively

positive OLR anomaly around 100° E corresponded to the area of the anticyclone (Fig. 2). The pair of OLR anomalies can be traced back to the area around 160° E. Similar westward movements of areas of active and suppressed convection occurred repeatedly with a 10–20-day period (i.e., QBW ISO) from mid-August to the end of September. They were associated with ISO signals with a ~ 10-day period, which were particularly active in September over the Bay of Bengal (Fig. S4). These signals crossed the Indian subcontinent and reached the Arabian Sea only in late September around the time of the extreme event. There is close agreement between the westward-moving and ER-filtered OLR anomalies (Fig. 3a). Moreover, the streamfunction and wind anomaly field exhibit the typical structure of $n = 1$ ER waves with a wavenumber of ~ 4, which is characterized by westward propagating twin vortices (i.e., twin lows or highs) with centers around ~ 15° N and ~ 0° at 60°–150° E (Fig. 3c) (Chatterjee and Goswami 2004; Fujinami et al. 2014). The QBW ISO appears to have promoted the occurrence of the LPS around the Bay of Bengal and the subsequent anticyclone (Hatsuzuka and Fujinami 2017) although a discussion of the detailed mechanisms is outside the scope of this study. Meanwhile, the boreal summer intraseasonal oscillation (BSISO) with a 25–90-day period (Kikuchi 2021) did not show a pronounced northward progression into the Bay of Bengal during summer 2024 and thus had little impact on the extreme precipitation event (Fig. S5). It has been noted that heavy rainfall in Nepal occurs during the break phase of BSISO (Bohlinger et al. 2017, 2019), but reports of heavy rainfall events in Nepal involving QBW ISO are extremely rare. By contrast, QBW ISO strongly influences precipitation variability and extreme rainfall events in the Bay of Bengal and Bangladesh region (Fujinami et al. 2014, 2017; Murata et al. 2017).

3.2 Mesoscale precipitation/cloud systems and precipitation characteristics

Mesoscale cloud/precipitation systems are embedded within the synoptic-scale convective activity shown in Fig. 2. Figure 4 shows the mesoscale cloud/precipitation systems on 27–28 September, when heavy rainfall occurred over central–eastern Nepal, including the Rolwaling/Khumbu regions. At 09:00–12:00 UTC on 27 September, tall convective clouds with brightness temperatures of < 220 K developed on the windward side away from the Himalayan slopes (Fig. 4a and b). Lower-level broad areas of cloud with brightness temperatures of < 240 K covered the Himalayan slopes. Between 12:00 and 18:00 UTC, the convective cloud cluster that was at approximately 25° N, 80° E at 12:00 UTC evolved into a single widespread convective cloud shield as it approached the Himalayan slopes (Fig. 4b–d). The shield further extended toward the southern end of the concave slopes over approximately 4 h (18:00–22:00 UTC) (Fig. 4e). During this period, WVF was perpendicular to the Himalayan slopes. Subsequently, the shield broke up and part of it moved northward over the slopes (Fig. 4f). At 00:00 UTC on 28 September, when the WVF shifted from southwesterly to west-southwesterly, a new area of convective cloud formed immediately west of

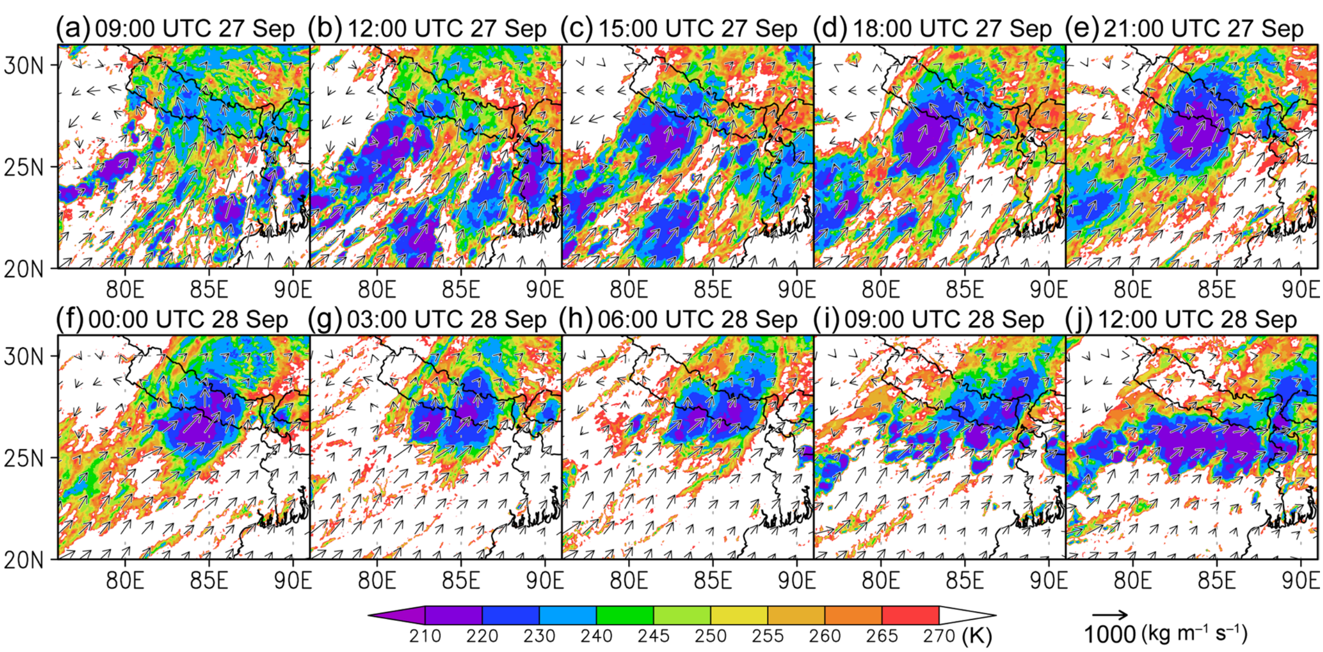

Fig. 4 (**a**)–(**e**) Distribution of infrared brightness temperature from Meteosat-9 (shading; K) and integrated water vapor flux (vectors; kg m^{-1} s^{-1}) at 3-h intervals from 09:00 UTC on 27 September to 12:00 UTC on 28 September 2024

the shield. The two relatively extensive areas of convective cloud then advanced eastward during 03:00–06:00 UTC (Fig. 4g and h). The convective clouds appeared to pass over the Rolwaling/Khumbu regions between 03:00 and 12:00 UTC. After 09:00 UTC, the convective clouds were aligned linearly, extending along an east–west axis away from the Himalayas (Fig. 4i and j).

On 27 September, the GPM core observatory passed over Nepal twice (Fig. 5). According to GPM data, scattered convective cloud systems that were around 25° N, 80° E at approximately 12:00 UTC were associated with rainfall of > 20 mm h^{-1} (Fig. 5a and b). These areas of intense precipitation exhibited a high convective rain fraction (> 80%), with storm top height exceeding 10 km asl (Fig. 5c and d). Over the Himalayas, intense precipitation of > 10 mm h^{-1} was observed in some areas, although storm top heights were below 10 km asl and convective rainfall fraction was low (i.e., high stratiform rain fraction). At 21:00 UTC, when the extensive convective cloud shield appeared south of the Himalayas, precipitation of > 100 mm h^{-1} was observed over the concave slopes in central Nepal. However, this extremely heavy rainfall was not associated with a particularly high storm top height; it was associated with a stratiform-type system with a storm top height of < 10 km. Furthermore, precipitation on the slopes was not provided by the precipitation system associated with the convective cloud shield. This cloud shield was an anvil cloud that was associated with a tall convective precipitation system near 26° N, 83° E, which was far from the Himalayan slopes (Fig. 5e and f).

Differences between the precipitation systems over the Himalayas and those over the plain south of the Himalayas can be seen in vertical cross sections of precipitation rate (Fig. 6). The precipitation systems over the plain south of the Himalayas involved deep convection, with storm top heights reaching 15 km (Fig. 6a and b). By contrast, over the Himalayan slopes, heavy precipitation was confined to elevations of < 5 km, and storm top heights were lower than those associated with deep convection. The most striking feature is the increase of precipitation rate with decreasing elevation, which indicates efficient generation of heavy precipitation by warm rain processes (Hamada et al. 2015). As shown previously, the synoptic-scale atmospheric circulation created very moist conditions around the Himalayas during this event. The substantial WVF continuously supplied large amounts of water vapor toward the Himalayas.

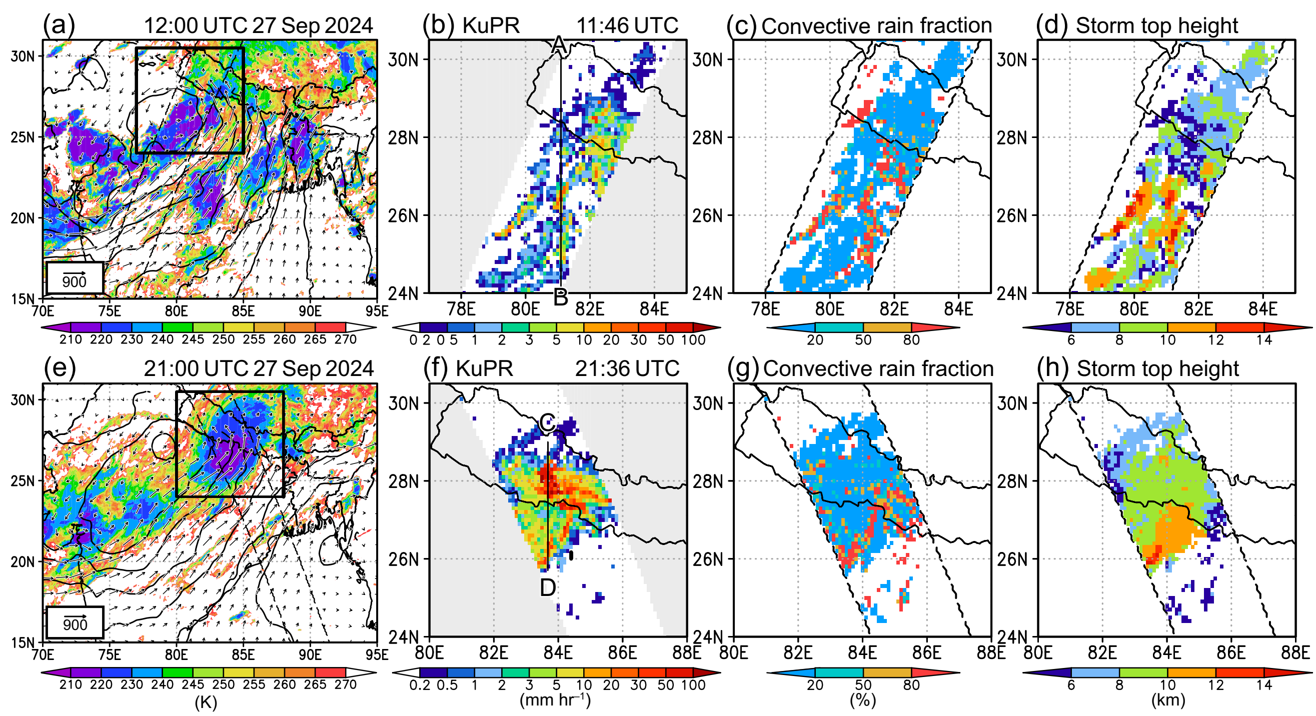

Fig. 5 (**a**) Spatial distribution of infrared brightness temperature from Meteosat-9 (shading; K), integrated water vapor flux (vectors; kg m^{-1} s^{-1}), and 850-hPa geopotential height (contours; gpm) at 12:00 UTC on 27 September 2024. Area enclosed between the diagonal dashed lines indicates the swath of the Global Precipitation Measurement Dual-frequency Precipitation Radar Ku-band product (GPM KuPR). Details for the area enclosed in the box are shown in (**b**)–(**d**). (**b**) Near-surface precipitation rate from GPM KuPR (mm h^{-1}) at 11:46 UTC on 27 September. Area with white shading indicates the GPM KuPR swath. (**c**) As in (**b**) but for convective rain fraction (shading; %). Area enclosed between the dashed lines indicates the GPM KuPR swath. (**d**) As in (**c**) but for storm top height (shading; km). (**e**) As in (**a**) but for 21:00 UTC on 27 September. Details for the area enclosed in the box are shown in (**f**)–(**h**). (**f**)–(**h**) As in (**b**)–(**d**), respectively, but for 21:36 UTC on 27 September. Lines A–B and C–D indicate the locations for the height–latitude sections in Fig. 6

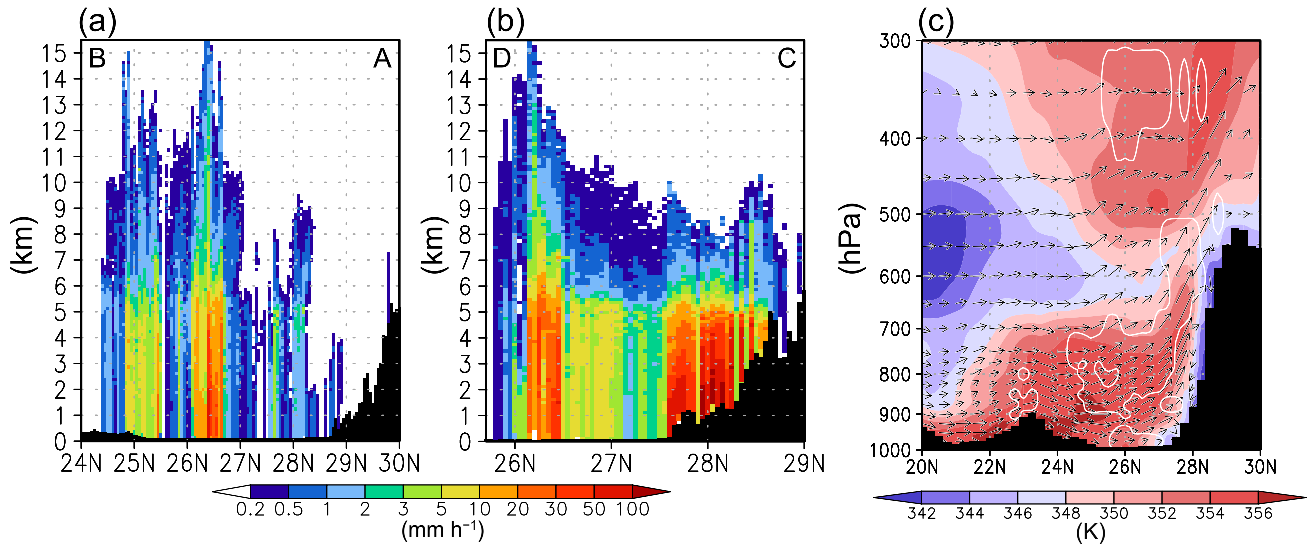

Fig. 6 (**a**) Height–latitude section of precipitation rate (shading in colors except black; mm h^{-1}) along line A–B (Fig. 5**b**) from the Global Precipitation Measurement Dual-frequency Precipitation Radar Ku-band product (GPM KuPR) at 11:46 UTC on 27 September 2024. Black shading indicates elevation from Global Multi-resolution Terrain Elevation Data (GMTED2010). (**b**) As in (a) but for line C–D (Fig. 5**f**) at 21:36 UTC. (**c**) Height–latitude section of equivalent potential temperature (shading in colors except black; K) and meridional and vertical winds (vectors; vertical wind is multiplied by 10) between 83° and 83.75° E at 21:00 UTC on 27 September 2024. Areas enclosed by white contour meet the moist absolutely unstable layer (MAUL) criteria (see text for details). Black shading indicates elevation from European Centre for Medium-Range Weather Forecasts Reanalysis fifth-generation (ERA5) data

Owing to the deep convective activity in the windward area of the Himalayas, humidity increased at all elevations up to the mid-troposphere. These phenomena, together with the continuous forced uplift of very moist air over the Himalayan slopes suggest the existence of a moist absolutely unstable layer (MAUL) around the Himalayas (Bryan and Fritsch 2000). Following Takemi and Unuma (2020), we identified MAULs as areas with a negative vertical gradient in equivalent potential temperature and relative humidity of ≥99%. Figure 6c shows that the air layer rising over the Himalayan slopes meets the criteria for a MAUL. In MAULs, heavy precipitation can be maintained without very deep convection (Tsuji et al. 2020, 2021).

3.3 Extreme precipitation at higher elevations

At the higher elevations of > 3000 m, precipitation is dependent on elevation and typically decreases with increasing elevation (Fujinami et al. 2021; Hirata et al. 2023). In the Rolwaling and Khumbu regions, the daily and hourly precipitation rates for 27 and 28 September (hereafter, 27/8) were higher than usual. Daily precipitation rates during 27/8 far exceeded the upper whisker of the box plot in summer (June–September) 2024. Substantial positive deviations from summer precipitation values were recorded at stations that were higher than Beding station (3761 m) (Figs. 7a and S6a–e). We expressed the cumulative precipitation from 27/8 as a percentage of the total summer precipitation in 2024. Results show that the percentage increased with elevation between Beding and Trakarding Glacier (4806 m) stations and exceeded 20% at Na and Trakarding Glacier stations (Fig. 7a).

The characteristics of hourly precipitation rate are similar to those of daily precipitation (Fig. 7b). At stations that were higher than Beding station, hourly precipitation rates during 27/8 were higher than usual (Figs. 7b and S6f–j), exceeding the upper whisker in summer 2024 at several stations. Elevation dependence was present across mean summer rates (cross marks in Fig. 7b) but absent from hourly rates during 27/8 (circles in Fig. 7b). Comparisons with summer data from 2024 (Fig. 7) and 2016–2019 (Fig. S7) from the Rolwaling region confirm that precipitation rates during 27/8 were exceptionally high, especially at elevations of > 3761 m (Fujinami et al. 2021; Hirata et al. 2023).

4 Conclusions

This study investigated the multiscale factors contributing to the extreme precipitation event in Nepal at the end of September 2024 by examining the synoptic-scale circulation fields, ISOs, and mesoscale cloud/precipitation systems around the Himalayas. The synoptic-scale atmospheric circulation during this period was characterized by an LPS over the Indian Peninsula, together with an anticyclone to its east. The anticyclone exhibited a barotropic-like structure.

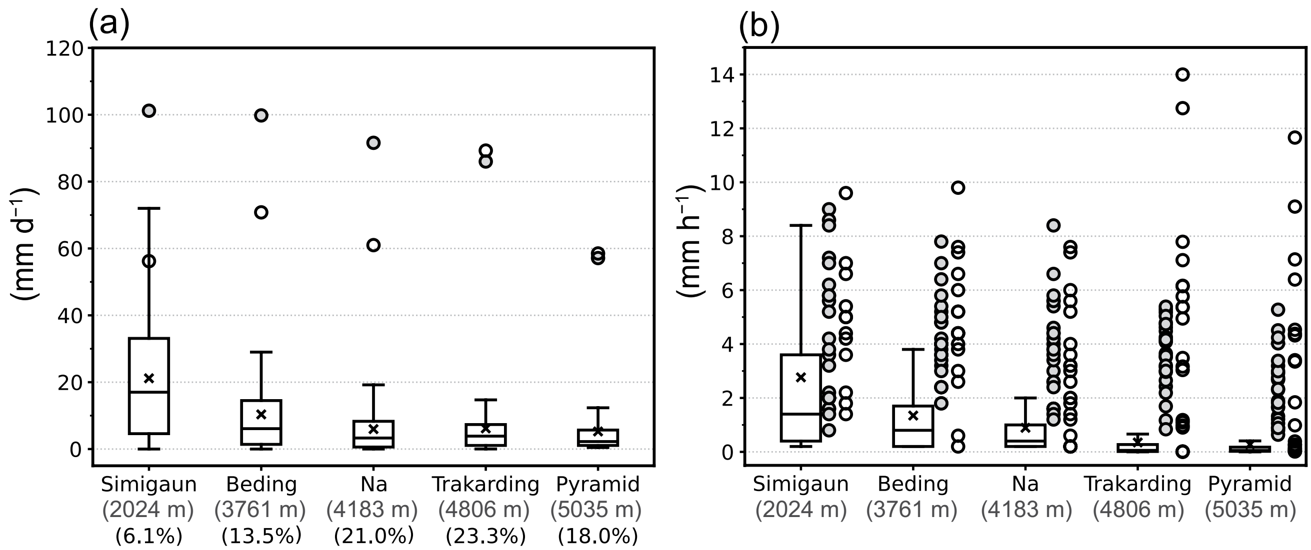

Fig. 7 (**a**) Boxplots of daily precipitation (mm d^{-1}) based on rain gauge data from the Simigaun, Beding, Na, and Trakarding Glacier stations in the Rolwaling region and the Pyramid observatory in the Khumbu region for 1 June to 30 September 2024. The box represents the interquartile range (25th −75th percentiles), with the horizontal line indicating the median. The cross mark denotes the mean value. The whiskers extend to 1.5 times the interquartile range. Gray and open circles above the boxplot indicate daily precipitation for 27 and 28 September, respectively, for each station. The elevation (m asl) of each location is shown in parentheses below the station name, along with the cumulative precipitation from 27 and 28 September expressed as a percentage of the total precipitation from June–September. (**b**) As in (**a**) but based only on hourly precipitation of > 0 mm h^{-1}. Gray and open circles immediately to the right of the boxplot represent hourly precipitation on 27 and 28 September, respectively, for each station

The occurrence and movement of these two synoptic-scale systems were controlled by a QBW ISO, which originated in the tropics and was on a larger spatiotemporal scale. By contrast, the influence of the midlatitude circulation, which has been commonly reported as the primary cause of many past heavy rainfall events, remained weak throughout the 2024 event. The involvement of QBW ISO continuously generated a pressure gradient that sustained a large southerly WVF to the southern Himalayas from the lower to the middle troposphere. This created an extremely humid environment around the southern Himalayan slopes and led to continuous forced uplift of humid air along the slopes throughout the event.

Under these synoptic-scale conditions, characteristic mesoscale cloud/precipitation systems appeared around the Himalayas. On 27 September, the wind direction became perpendicular to the slope, leading to enhanced WVF convergence along the concave slopes of central Nepal; the highest daily total precipitation during the event was recorded on this day. To the south of the Himalayas, deep convective-type cloud/precipitation systems brought precipitation with moderate intensity. By contrast, stratiform-type precipitation systems with moderate storm top height and high precipitation intensity developed over the southern slopes of the Himalayas, delivering surface precipitation rates that exceeded 100 mm h^{-1}. Vertical profiles of the precipitation over the slopes indicate the increase of rainfall intensity with decreasing elevation. This suggests efficient formation of precipitation through warm rain processes associated with a large inflow of water vapor and continuous forced uplift of a very moist layer along the Himalayan slopes, similar to a MAUL. On 28 September, the westerly component strengthened south of the Himalayas. The strong convective cloud/precipitation system moved northeastward, bringing substantial precipitation to the Himalayas at higher elevations, including to glacierized areas.

Data from the rain gauge network deployed in the glacierized basin in eastern Nepal show that daily and hourly precipitation rates were abnormally high during this event, particularly in areas above 3500 m asl. While both daily and hourly precipitation rates typically decrease with increasing elevation, these elevation dependencies were not observed during this event.

Further analysis is required to understand the mechanism by which QBW ISO generated the synoptic-scale LPS over the Bay of Bengal in this event. Detailed analysis using cloud-resolving models is also needed to understand how mesoscale precipitation systems form and develop over the Himalayan slopes. To assess whether events like the one in 2024 will become more frequent under global warming, further climatological studies are necessary. Assessing the influence of extreme precipitation events on glacier mass balance is also an important topic for future research.

Supplementary Information The online version contains supplementary material available at https://doi.org/10.1007/s44393-026-00024-0.

Acknowledgements This work was supported by the Japan Society for the Promotion of Science (JSPS) (KAKENHI Grants: 22H00176, 22H00033, 22H00037, and 23KK0064). It was partly supported by the 4th Research Announcement on the Earth Observations of the Japan Aerospace Exploration Agency (JAXA). It was partly carried out under the joint research program of Institute for Space–Earth Environmental Research, Nagoya University and as a joint research program with the Center for Environmental Remote Sensing (CEReS), Chiba University (CJ25-43, 2025). We thank James Buxton MSc and Tina Tin PhD from Edanz (https://jp.edanz.com/ac), for editing a draft of this manuscript.

Author contributions All authors contributed to the concept and design of the study. Data collection was performed by Hironari Kanamori, Koji Fujita, Yota Sato, Sojiro Sunako, Dibas Shrestha, Indira Kadel, and Rijan B. Kayastha. Analysis was performed by Hatsuki Fujinami, Nobuhiro Takahashi, and Hironari Kanamori. The first draft of the manuscript was written by Hatsuki Fujinami and all authors commented on the manuscript. All authors have read and approved the final manuscript.

Funding The Japan Society for the Promotion of Science (JSPS) supports this work (KAKENHI Grants: 22H00176, 22H00033, 22H00037, and 23KK0064).

Data Availability Daily rainfall data across Nepal were obtained from the Department of Hydrology and Meteorology, Kathmandu, Nepal (https://dhm.gov.np/). Precipitation data from Pyramid observatory are available from [https://glacioclim.osug.fr/Donnees-du-Nepal-region-du-Khumbu](https:/glacioclim.osug.fr/Donnees-du-Nepal-region-du-Khumbu) . Precipitation data from rain gauges in Rolwaling valley are available from https://doi.org/10.5281/zenodo.18081206. NOAA's Climate Prediction Center provided daily OLR data ([https://psl.noaa.gov/data/gridded/data.cpc_blended_olr-2.5 deg.html](https:/psl.noaa.gov/data/gridded/data.cpc_blended_olr-2.5 deg.html)). We used infrared brightness temperature data from MSG2 (Meteosat 9)-IODC. The Center for Environmental Remote Sensing (CEReS), Chiba University, archived and provided the data (https://ceres.chiba-u.jp/en/top-eng/). The GPM DPR products are available from the Japan Aerospace Exploration Agency (JAXA) G-Portal website ([https://gportal.jaxa.jp/gpr/](https:/gportal.jaxa.jp/gpr)). The ERA5 data are available from the Copernicus climate-change service (C3S) climate data store (https://doi.org/10.24381/cds.bd0915c6). GMTED2010 data are avail able from the US Geological Survey (https://topotools.cr.usgs.gov/gmted_viewer/viewer.htm).

Declarations

Competing interests The authors declare no competing interests.

References

Awaka J, Le M, Brodzik S, Kubota T, Masaki T, Chandrasekar V, Iguchi T (2021) Development of precipitation type classification algorithms for a full scan mode of GPM dual-frequency precipitation radar. J Meteorol Soc Jpn 99:1253–1270. https://doi.org/10.2151/jmsj.2021-061

Bohlinger P, Sorteberg A, Sodemann H (2017) Synoptic conditions and moisture sources actuating extreme precipitation in Nepal. J Geophys Res: Atmos 122:12653–12671. https://doi.org/10.1002/2017JD027543

Bohlinger P, Sorteberg A, Liu C, Rasmussen R, Sodemann H, Ogawa F (2019) Multiscale characteristics of an extreme precipitation event over Nepal. Q J R Meteorol Soc 145:179–196. https://doi.org/10.1002/qj.3418

Bolton D (1980) The computation of equivalent potential temperature. Mon Weather Rev 108:1046–1053. https://doi.org/10.1175/1520-0493(1980)108%3C1046:TCOEPT%3E2.0.CO;2

Bryan GH, Fritsch JM (2000) Moist absolute instability: The sixth static stability state. Bull Am Meteorol Soc 81:1207–1230. https://doi.org/10.1175/1520-0477(2000)081%3C1287:MAITSS%3E2.3.CO;2

Chatterjee P, Goswami BN (2004) Structure, genesis and scale selection of the tropical quasi-biweekly mode. Q J R Meteorol Soc 130:1171–1194. https://doi.org/10.1256/qj.03.133

Das S, Ashrit R, Moncrieff MW (2006) Simulation of a Himalayan cloudburst event. J Earth Syst Sci 115:299–313. https://doi.org/10.1007/BF02702044

Department of Hydrology and Meteorology (DHM) (2024) Situational report on extreme precipitation and flooding event of 27–29 September 2024. Government of Nepal. https://www.dhm.gov.np/uploads/dhm/downloads/Situational_Report_on_Extreme_Precipitation_and_Flooding_Event_of_27-29_September_2024.pdf. Accessed 9 October 2024

Dimri AP, Chevuturi A, Niyogi D, Thayyen RJ, Ray K, Tripathi SN, Pandey AK, Mohanty UC (2017) Cloudbursts in Indian Himalayas: A review. Earth-Sci Rev 168:1–23. https://doi.org/10.1016/j.earscirev.2017.03.006

Duchon CE (1979) Lanczos filtering in one and two dimensions. J Appl Meteorol 18:1016–1022

Fujinami H, Yasunari T, Morimoto A (2014) Dynamics of distinct intraseasonal oscillation in summer monsoon rainfall over the Meghalaya–Bangladesh–western Myanmar region: Covariability between the tropics and mid-latitudes. Clim Dyn 43:2147–2166. https://doi.org/10.1007/s00382-013-2040-1

Fujinami H, Sato T, Kanamori H, Murata F (2017) Contrasting features of monsoon precipitation around the Meghalaya Plateau under westerly and easterly regimes. J Geophys Res: Atmos 122:9591–9610. https://doi.org/10.1002/2016JD026116

Fujinami H, Fujita K, Takahashi N, Sato T, Kanamori H, Sunako S, Kayastha RB (2021) Twice-daily monsoon precipitation maxima in the Himalayas driven by land surface effects. J Geophys Res: Atmos 126. https://doi.org/10.1029/2020JD034255. e2020JD034255

Fujinami H, Sugimoto S, Ueno K (2025) Dynamics of rainstorms over southern Himalayan slopes and foothills and their simulation by numerical models. In: Das S, Tao WK (eds) Severe storms: Anatomy, early warning systems and aftermath in changing climate scenarios. Springer, Singapore, pp 333–359. https://doi.org/10.1007/978-981-97-7075-5_13

Hamada A, Takayabu YN, Liu C, Zipser EJ (2015) Weak linkage between the heaviest rainfall and tallest storms. Nat Commun 6:6213. https://doi.org/10.1038/ncomms7213

Hatsuzuka D, Fujinami H (2017) Effects of the south Asian monsoon intraseasonal modes on genesis of low pressure systems over

Bangladesh. J Clim 30:2481–2499. https://doi.org/10.1175/JCLI-D-16-0360.1
Hersbach H, Bell B, Berrisford P, Hirahara S, Horányi A, Muñoz-Sabater J, Nicolas J, Peubey C, Radu R, Schepers D, Simmons A, Soci C, Abdalla S, Abellan X, Balsamo G, Bechtold P, Biavati G, Bidlot J, Bonavita M, De Chiara G, Dahlgren P, Dee D, Diamantakis M, Dragani R, Flemming J, Forbes R, Fuentes M, Geer A, Haimberger L, Healy S, Hogan RJ, Hólm E, Janisková M, Keeley S, Laloyaux P, Lopez P, Lupu C, Radnoti G, de Rosnay P, Rozum I, Vamborg F, Villaume S, Thépaut J-N (2020) The ERA5 global reanalysis. Q J R Meteorol Soc 146:1999–2049. https://doi.org/10.1002/qj.3803
Hirata H, Fujinami H, Kanamori H, Sato Y, Kato M, Kayastha RB, Shrestha ML, Fujita K (2023) Multiscale processes leading to heavy precipitation in the eastern Nepal Himalayas. J Hydrometeorol 24:641–658. https://doi.org/10.1175/JHM-D-22-0080.1
Houze RA Jr, McMurdie LA, Rasmussen KL, Kumar A, Chaplin MM (2017) Multiscale aspects of the storm producing the June 2013 flooding in Uttarakhand, India. Mon Weather Rev 145:4447–4466. https://doi.org/10.1175/MWR-D-17-0004.1
Kikuchi K (2021) The boreal summer intraseasonal oscillation (BSISO): A review. J Meteorol Soc Jpn 99:933–972. https://doi.org/10.2151/jmsj.2021-045
Kiladis GN, Wheeler MC, Haertel PT, Straub KH, Roundy PE (2009) Convectively coupled equatorial waves. Rev Geophys 47. https://doi.org/10.1029/2008RG000266. :RG2003
Lamichhane K, Biswakarma K, Acharya B, Karki S, KC R, Subedi M, Sharma K (2025) Preliminary assessment of September 2024 extreme rainfall–induced landslides in Central Nepal. Landslides 22:3281–3295. https://doi.org/10.1007/s10346-025-02577-w
Masunaga H (2007) Seasonality and regionality of the Madden–Julian oscillation, Kelvin wave, and equatorial Rossby wave. J Atmos Sci 64:4400–4416. https://doi.org/10.1175/2007JAS2179.1
Murata F, Terao T, Fujinami H, Hayashi T, Asada H, Matsumoto J, Syiemlieh HJ (2017) Dominant synoptic disturbance in the extreme rainfall at Cherrapunji, North East India based on 100 years of rainfall data. J Clim 30:8237–8251. https://doi.org/10.1175/JCLI-D-16-0435.1
Schmetz J, Pili P, Tjemkes S, Just D, Kerkmann J, Rota S, Ratier A (2002) An introduction to Meteosat Second Generation (MSG). Bull Am Meteorol Soc 83:977–992. https://doi.org/10.1175/1520-0477(2002)083%3C0977:AITMSG%3E2.3.CO;2
Seto S, Iguchi T, Meneghini R, Awaka J, Kubota T, Masaki T, Takahashi N (2021) The precipitation rate retrieval algorithms for the GPM dual-frequency precipitation radar. J Meteorol Soc Jpn 99:205–237. https://doi.org/10.2151/jmsj.2021-011
Sharma S, Chen Y, Zhou X, Yang K, Li X, Niu X, Hu X, Khadka N (2020) Evaluation of GPM-era satellite precipitation products on the southern slopes of the Central Himalayas against rain gauge data. Remote Sens 12:1836. https://doi.org/10.3390/rs12111836
Takemi T, Unuma T (2020) Environmental factors for the development of heavy rainfall in the eastern part of Japan during typhoon Hagibis (2019). SOLA 16:30–36. https://doi.org/10.2151/sola.2020-006
Talchabhadel R, Ghimire GR, Sharma S, Dahal P, Panthi J, Baniya R, Pudashine J, Thapa BR, PC S, Parajuli B (2022) Weather radar in Nepal: Opportunities and challenges in a mountainous region. Weather 77:160–164. https://doi.org/10.1002/wea.3994
Tsuji H, Yokoyama C, Takayabu YN (2020) Contrasting features of the July 2018 heavy rainfall event and the 2017 northern Kyushu rainfall event in Japan. J Meteorol Soc Jpn 98:859–876. https://doi.org/10.2151/jmsj.2020-045
Tsuji H, Takayabu YN, Shibuya R, Kamahori H, Yokoyama C (2021) The role of free-tropospheric moisture convergence for summertime heavy rainfall in western Japan. Geophys Res Lett 48. https://doi.org/10.1029/2021GL095030. e2021GL095030
Vellore RK, Kaplan ML, Krishnan R, Lewis JM, Sabade S, Deshpande N, Singh BB, Madhura RK, Rama Rao MV (2016) Monsoon-extratropical circulation interactions in Himalayan extreme rainfall. Clim Dyn 46:3517–3546. https://doi.org/10.1007/s00382-015-2784-x